fractal and fractional

Article

A Fractional-Order ADRC Architecture for a PMSM Position Servo System with Improved Disturbance Rejection

Shaohua Wang [1], He Gan [1], Ying Luo [2,*], Xin Luo [1] and Yangquan Chen [3]

1 School of Mechanical Science and Engineering, Huazhong University of Science and Technology, Wuhan 430074, China; shaohua94@hust.edu.cn (S.W.); hegan@hust.edu.cn (H.G.); mexinluo@hust.edu.cn (X.L.)
2 School of Automation Science and Engineering, South China University and Technology, Guangzhou 510641, China
3 The Mechatronics, Embedded Systems and Automation Lab, Department of Mechanical Engineering, School of Engineering, University of California, Merced, CA 95343, USA; ychen53@ucmerced.edu
* Correspondence: yingluosase@scut.edu.cn

Abstract: This paper proposes an active disturbance rejection control (ADRC) architecture for a permanent magnet synchronous motor (PMSM) position servo system. The presented method achieved enhanced tracking and disturbance rejection performance with a limited observer bandwidth. The model-aided extended state observer (MESO)-based ADRC was designed for the current, speed, and position loops of the PMSM position servo system. By integrating known plant information, the MESO improved disturbance estimation with a limited observer bandwidth without amplifying the noise. Additionally, a fractional-order proportional-derivative (FOPD) controller was designed as the feedback controller for the speed loop to further enhance the disturbance rejection. A simulation and experimental tests were conducted on a PMSM servo platform. The results demonstrate not only that the proposed method achieved superior tracking performance but also that the position error of the proposed strategy decreases to 2.25% when the constant disturbance was input, significantly improving the disturbance rejection performance.

Keywords: fractional-order control; active disturbance rejection control; extended state observer; PMSM position servo system; disturbance rejection.

check for updates

Citation: Wang, S.; Gan, H.; Luo, Y.; Luo, X.; Chen, Y. A Fractional-Order ADRC Architecture for a PMSM Position Servo System with Improved Disturbance Rejection. *Fractal Fract.* **2024**, *8*, 54. https://doi.org/10.3390/fractalfract8010054

Academic Editors: Germán Ardúl Muñoz Hernández and Fermi Guerrero-Castellanos

Received: 27 November 2023
Revised: 28 December 2023
Accepted: 8 January 2024
Published: 14 January 2024

1. Introduction

Permanent magnet synchronous motors (PMSMs) have gained widespread use in industrial applications [1]. However, the existence of nonlinearities, uncertainties, and disturbances [2] makes it challenging for a conventional proportional–integral (PI) control strategy to achieve high-precision control for the PMSM servo system [3,4]. In recent years, diverse control strategies have been developed for PMSM, aiming to enhance control effectiveness. Active disturbance rejection control (ADRC) is one of the most popular control strategies.

Proposed in the 1980s by Jingqing Han [5], ADRC was designed to address extensive uncertainties and disturbances. The fundamental concept of ADRC involves treating external disturbances and internal uncertainties collectively as the “total disturbance”, which is then estimated using the extended state observer (ESO) and actively compensated for via the ESO-based feedback controller. Despite its theoretical soundness, the intricate nonlinear structure and intricate tuning process have rendered its practical application challenging. A linear version (LADRC) and bandwidth parameterization proposed by Zhiqiang Gao have greatly simplified the structures and tuning of ADRC [6]. As a result, ADRC can be quickly applied in various industrial areas, such as wind turbines [7], robot control [8], aerial vehicles [9,10], motor control [11], and so on. In recent years, the field of ADRC has undergone substantial growth.

LADRC possesses various superior properties, including a compact structure, model independence, superior disturbance rejection, and robustness [12,13]. However, there are still some challenges that necessitate additional research:

- A high observer bandwidth is required to achieve the desired disturbance estimation and rejection [6], but the high observer bandwidth will amplify the measurement noise [14].
- The LESO and the feedback controller are mutually coupled, while the tracking performance cannot be completely separated from the LESO [15,16].
- The design of LADRC based on the bandwidth parameterization method is relatively conservative, potentially leading to suboptimal control performance [17].

Various versions of ADRC have been proposed to tackle these challenges. Some studies designed ADRC to incorporate the known plant information to improve the disturbance rejection performance. For instance, the ADRC strategy with a generalized extended sta observer (GESO) was presented in [17–19], where the known plant information was incorporated into the ESO. With a GESO, ADRC shows improved control capability on non-minimum-phase, unstable, and time-delay systems. Another benefit of GESO-based ADRC demonstrated in [16] is that it satisfies the separation principle, meaning that the feedback controller design is separated from a GESO. Ref. [20] applied the ADRC with a model-aided ESO (MESO) in the current control of a PMSM, obtaining enhanced parameter robustness performance. Some studies have modified the structure of ADRC to improve the control performance. Ref. [14] presented an improved ESO to suppress the measurement noise. Recently, some intelligent algorithms have been applied in ADRC. Ref. [21] applied a diagonal recurrent neural network in ADRC for the radar position servo system facing a dead zone and friction nonlinearities. Ref. [22] introduced an ADRC method based on the deep reinforcement learning algorithm for more electric aircraft. Ref. [23] presented an optimal ADRC based on a proportional-derivative (PD) control law with particle swarm optimization to improve the dynamic and steady-state control performance.

In recent developments, integrating ADRC with fractional-order control (FOC) has garnered attention to enhance control performance. FOC is the extension of traditional integer-order control, providing more flexibility in controller design and improved control performance [24]. An application of fractional-order ADRC (FOADRC) was presented for a linear motor to achieve precise tracking performance [25]. Ref. [16] proposed an FOADRC controller with GESO to improve tracking and disturbance rejection performance for a PMSM servo system. The design of FOADRC with fractional-order ESO was investigated in [26] to suppress noise sensitivity. Ref. [27] proposed a fractional-order ESO-based ADRC method to address the trade-off between control performance and noise suppression. Ref. [28] presented a fractional-order ADRC method incorporating the fuzzy self-tuning method, which achieved an improved dynamic response and disturbance suppression capability. Ref. [29] proposed an optimal fractional-order ADRC method for the PMSM speed servo system, which met the requirement for frequency-domain indicators and achieved optimal performance in the time domain. A comparison of these versions of ADRC is presented in Table 1.

The primary objective of this paper is to improve the disturbance rejection performance with an observer bandwidth limitation for the PMSM position servo system, integrating the benefits of the model-aided ADRC and fractional-order control. The primary contributions of this paper are summarized as follows:

(1) An MESO-based ADRC architecture is introduced for the PMSM position servo system, demonstrating improved tracking and disturbance rejection under limited observer bandwidth.
(2) The MESO-based ADRC was designed for the current, speed, and position loops. Additionally, a fractional-order feedback controller was designed for the speed loop, further enhancing the disturbance rejection performance on the basis of the MESO.
(3) Simulation and experimental comparison tests on a PMSM position servo system were conducted to verify the effectiveness of the proposed method.

Table 1. Comparison of different versions of ADRC.

References	Linear/Nonlinear	ESO	Feedback Controller
[5]	Nonlinear	Nonlinear ESO	Error-Based Nonlinear Controller
[6]	Linear	LESO	State Feedback Controller
[14]	Linear	Improved ESO	State Feedback Controller
[17–19]	Linear	GESO	State Feedback Controller
[16]	Linear	GESO	Fractional-Order PD
[20]	Linear	Model-Aided ESO	Model Predictive Control
[25]	Nonlinear	Nonlinear ESO	Fractional-order PD
[29]	Linear	LESO	Fractional-Order PD
[26,27]	Linear	FOESO	PID
[28]	Linear	FOESO	Fuzzy Self-Tuning PD

The subsequent sections of this paper are organized as follows: In Section 2, the MESO-based ADRC is presented. Section 3 covers the design and tuning of the cascade ADRC strategy for the PMSM position servo system. Simulation comparisons and a discussion are presented in Section 4. Section 5 presents experimental verification. Finally, Section 6 presents the conclusion of this paper.

2. The Principle of MESO-Based ADRC

Figure 1 illustrates the structure of the MESO-based ADRC. It comprises an MESO and a feedback controller. The controlled plant is an n-th order system. The MESO estimates the lumped disturbance and plant states in real time. The feedback controller and MESO collaborate to generate the control effort. The specific details of the MESO-based ADRC are described below.

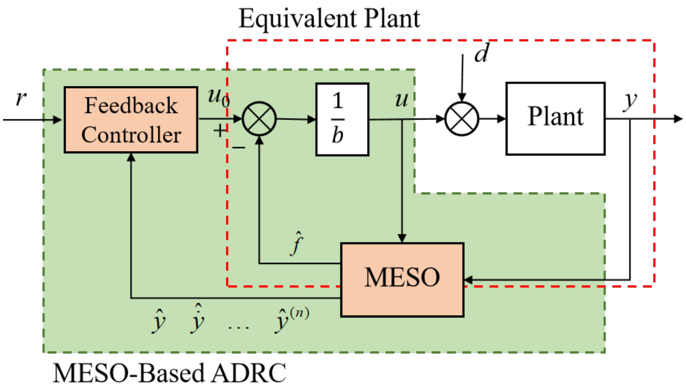

Figure 1. Block diagram of MESO-based ADRC.

2.1. MESO-Based ADRC

Consider an n-th order plant:

$$y^{(n)} + a_{n-1}y^{(n-1)} + \cdots + a_1\dot{y} + a_0 = bu + d, \tag{1}$$

where y, u, and d are the plant's output, input, and external disturbance, respectively; n is the order of the plant, and a_i $(i = 0, 1, 2, \ldots, n-1)$ and b are the plant coefficients. Its transfer function model is

$$P(s) = \frac{b}{s^n + a_{n-1}s^{n-1} + \cdots + a_1 s + a_0}. \tag{2}$$

Let f represent the lumped disturbance as

$$f = -a_{n-1}y^{(n-1)} - \cdots - a_1\dot{y} - a_0 y + d, \tag{3}$$

the plant (1) is converted to

$$y^{(n)} = f + bu. \tag{4}$$

The lumped disturbance f encompasses the known dynamics of the controlled plant and the unknown external disturbance.

When f is taken as an augmented state and $x = [y \ \ \dot{y} \ \ \ldots \ \ y^{n-1} \ \ f]^T$, $h = \dot{d}$ is defined (assuming d is differentiable), the plant (4) is represented as augmented state-space form:

$$\begin{cases} \dot{x} = Ax + Bu + Eh \\ y = Cx \end{cases}, \tag{5}$$

where

$$A = \begin{bmatrix} 0 & 1 & 0 & \cdots & 0 \\ 0 & 0 & 1 & \cdots & 0 \\ \vdots & \vdots & \vdots & \ddots & \vdots \\ 0 & 0 & 0 & \cdots & 1 \\ 0 & -a_0 & -a_1 & \cdots & -a_{n-1} \end{bmatrix}, B = \begin{bmatrix} 0 \\ 0 \\ \vdots \\ b \\ -a_{n-1}b \end{bmatrix},$$
$$E = \begin{bmatrix} 0 & 0 & \cdots & 0 & 1 \end{bmatrix}^T, C = \begin{bmatrix} 1 & 0 & \cdots & 0 & 0 \end{bmatrix}.$$

The MESO can be designed based on Equation (5) as

$$\begin{cases} \dot{\hat{x}} = A\hat{x} + Bu + L(y - \hat{y}) \\ \hat{y} = C\hat{x} \end{cases}, \tag{6}$$

where $\hat{x}$ is the estimation of x, $\hat{y}$ is the estimation of y, and L is the observer gain vector,

$$L = [\beta_1 \ \ \beta_2 \ \ \ldots \ \ \beta_n \ \ \beta_{n+1}]^T. \tag{7}$$

Remark 1. *The distinction between an MESO and an LESO lies in an MESO's utilization of all known plant information, while an LESO does not incorporate this information. The GESO proposed in [17] also utilizes known plant information, but it does not consider the known plant dynamics as part of the lumped disturbance f defined in the GESO. The GESO's disturbance compensation cannot transform the controlled plant into the ideal cascade integral plant. In contrast, an MESO can achieve cascade-integral plant equivalence because the known plant dynamics are considered as part of the lumped disturbance f in the MESO.*

The control effort is generated for the combination of the estimated disturbance $\hat{f}$ and the output of the feedback controller u_0 in real time, which is represented as

$$u = \frac{-\hat{f} + u_0}{b}, \tag{8}$$

Substitute it in (4), and the plant (1) is equivalent to

$$y^{(n)} = f - \hat{f} + u_0 \approx u_0. \tag{9}$$

If the MESO is designed appropriately, $\hat{f}$ completely compensates for the effects of the lumped disturbance f. Thus, the controlled plant is equivalent to an nth-order integrator plant. The state-feedback control law is designed as

$$u_0 = k_1(r - \hat{x}_1) - k_2\hat{x}_2 - \cdots - k_n\hat{x}_n. \tag{10}$$

In summary, the MESO-based ADRC can be expressed as

$$\begin{cases} \dot{\hat{x}} = (A - LC)\hat{x} + Bu + Ly, \\ u = K(\hat{r} - \hat{x}). \end{cases} \tag{11}$$

where $\hat{r} = [r \ \ 0 \ \ \ldots \ \ 0]^T$, $K = [K_0 \ \ 1]/b$, and $K_0 = [k_1 \ \ k_2 \ \ \ldots \ \ k_n]$.

2.2. Parameter Tuning

From (11), the MESO-based ADRC has two sets of gains to tune: the observer gain L and the state-feedback gain K. Many different methods can be utilized to tune L and K. The idea of the bandwidth parameterization method places all the poles of the ESO and the closed-loop system at $-\omega_o$ and $-\omega_c$ [6]. ω_o and ω_c are considered the bandwidths of the MESO and the closed-loop system.

Therefore, the characteristic equation of the MESO can be obtained using

$$|sI - (A - LC)| = (s + \omega_o)^{n+1}. \tag{12}$$

The value of β_i for L can be solved by comparing the coefficients of the two sides of (12).

Substitute (10) in (9), and the closed-loop system can be represented as

$$y^{(n)}(t) = k_1(r - \hat{x}_1) - k_2\hat{x}_2 - \cdots - k_n\hat{x}_n. \tag{13}$$

The characteristic equation of (13) can be expressed as

$$s^n + k_n s^{n-1} + \cdots + k_2 s + k_1 = (s + \omega_c)^n. \tag{14}$$

The value of k_i for K_0 can be solved from (14) as

$$k_i = C_n^{n+1-i}\omega_c^{n+1-i}. \tag{15}$$

Generally, the observer's response is faster than the closed-loop system's. Therefore, ω_o should be larger than ω_c, and an appropriate choice is $\omega_o = 2 \sim 6\omega_c$.

Remark 2. *The bandwidth parameterization method, while relatively conservative, facilitates the achievement of a non-overshoot response in the closed-loop system for setpoint tracking. In certain scenarios, there might be a need for a faster response. To address this, alternative tuning methods, including frequency specifications, loop shaping, and optimization, can be employed to attain the desired response. Moreover, various control laws, including PID, sliding mode control, and fractional-order control, can be implemented.*

2.3. Transfer Function Derivation

The MESO-based ADRC can be equivalent to a two-degrees-of-freedom closed-loop system, as shown in Figure 2, where $H(s)$ is the setpoint filter, and $C(s)$ is the feedback controller [30]. They can be obtained from the Laplace transform of (11) as follows:

$$C(s) = \frac{K[sI - (A - LC)]^{-1}L}{1 + K[sI - (A - LC)]^{-1}B}, \tag{16}$$

$$H(s) = \frac{k_1}{K[sI - (A - LC)]^{-1}L}. \tag{17}$$

From Figure 2, the transfer function from r to y is derived as follows:

$$G_{RY}(s) = \frac{H(s)C(s)P(s)}{1 + C(s)P(s)}. \tag{18}$$

It is used to derive the transfer function of the closed-loop system $G_{cl}(s)$. If $K_0 = 0$ is allowed, G_{RY} is converted to the equivalent plant $P_e(s)$.

The external disturbance transfer function $G_d(s)$ from d to y can be expressed as

$$G_{DY}(s) = \frac{P(s)}{1 + C(s)P(s)}. \tag{19}$$

It is used to analyze the disturbance rejection performance of the closed-loop system.

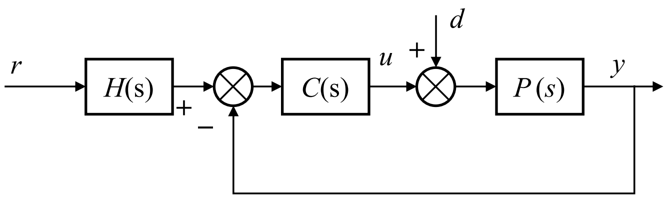

Figure 2. The transfer function form of the MESO-based ADRC

3. Cascade ADRC Strategy for a PMSM Position Servo System

The block diagram of the cascade ADRC for the PMSM position servo system is shown in Figure 3. There are three loops for the PMSM position servo system, i.e., current, speed, and position loops. The modeling of the PMSM and the MESO-based ADRC design for each loop is subsequently introduced.

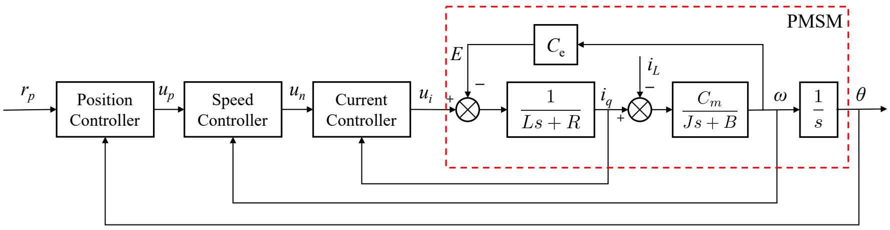

Figure 3. The structure of the cascade ADRC for a PMSM position servo system.

3.1. Modeling of PMSM

The voltage equations for a surface-mounted PMSM in d–q coordinates are expressed as follows:

$$\begin{cases} \frac{di_d}{dt} = \frac{1}{L_s}(-R_s i_d + n_p \omega L_s i_q + u_d) \\ \frac{di_q}{dt} = \frac{1}{L_s}(-R i_q - n_p \omega L_s i_d - n_p \psi_f \omega + u_q) \end{cases}, \tag{20}$$

where u_d, u_q, i_d, and i_q represent the stator voltages and currents of the d- and q-axes, respectively; L_s denotes the stator inductance, R_s is the stator resistance, ω signifies the angular velocity, n_p is the number of pole pairs, and ψ_f stands for the rotor flux linkage.

The current reference of the d-axis $i_d^* = 0$ is used to decouple the stator voltages and currents. Thus, the voltage equation represented by (20) is simplified to

$$\frac{di_q}{dt} = \frac{1}{L_s}(-R_s i_q - C_e \omega + u_q), \tag{21}$$

where $C_e = n_p \psi_f$ is the induced voltage constant.

The motion equation of the PMSM can be expressed as follows:

$$\begin{cases} \frac{d\omega}{dt} = \frac{1}{J}(C_m i_q - T_L - B_f \omega), \\ \frac{d\theta}{dt} = \omega. \end{cases} \tag{22}$$

where J is the moment of inertia, $C_m = 1.5 n_p \psi_f i_q$ is the torque coefficient, T_L is the load torque, B_f is the viscous friction coefficient, and θ is the mechanical angle of the rotor.

The transfer function model of the PMSM is obtained by applying the Laplace transform to Equations (21) and (22) under zero initial conditions as follows:

$$G_i(s) = \frac{1/L_s}{s + R_s/L_s}, \tag{23}$$

$$G_n(s) = \frac{C_m/J}{s + B_f/J}, \tag{24}$$

$$G_p(s) = \frac{1}{s}. \tag{25}$$

3.2. Current Loop Design

Taking the EMF as part of the lumped disturbance, the controlled plant for the current loop is $G_i(s)$, as in (23). According to (11), a first-order MESO-based ADRC can be designed for the current loop with $a_0 = R_s/L_s$ and $b = 1/L_s$.

The bandwidth parameterization method is adopted for the current loop. Given the observer bandwidth ω_{oi}, the observer gain $L_i = [\beta_1 \;\; \beta_2]^T$ is calculated using (12) as follows:

$$\begin{cases} \beta_1 = -a_0 + 2\omega_{oi}, \\ \beta_2 = (a_0 - \omega_{oi})^2. \end{cases} \tag{26}$$

Given the controller bandwidth ω_{ci}, the state feedback gain can be obtained using (14) as follows:

$$k_1 = \omega_{ci}. \tag{27}$$

The current closed loop can be obtained via (18) as follows:

$$G_{cli}(s) = \frac{\omega_{ci}}{s + \omega_{ci}}. \tag{28}$$

3.3. Speed Loop Design

The plant for the speed loop consists of the current closed loop (28) and the speed motion part (24), which can be represented as

$$P_n(s) = G_{cli}(s)G_n(s) = \frac{b}{s^2 + a_1 s + a_0}, \tag{29}$$

where $b = \frac{\omega_{ci}C_m}{J}$, $a_1 = \frac{\omega_{ci}J + B_f}{J}$, and $a_0 = \frac{\omega_{ci}B_f}{J}$.

The MESO for the speed loop can be designed based on (29). Given the observer bandwidth ω_{on}, the observer gain can be obtained via (12) as follows:

$$\begin{cases} \beta_1 = -a_1 + 3\omega_{on}, \\ \beta_2 = -a_0 + a_1^2 - 3a_1\omega_{on} + 3\omega_{on}^2, \\ \beta_3 = 2a_0a_1 - a_1^3 - 3a_0\omega_{on} + 3a_1^2\omega_{on} - 3a_1\omega_{on}^2 + \omega_{on}^3. \end{cases} \tag{30}$$

The equivalent plant for the speed loop can be obtained via (18) as follows:

$$P_{en}(s) = \frac{1}{s^2}. \tag{31}$$

Remark 3. *The equivalent plant is an ideal double-integrator plant equivalence, which means $P_{en}(s)$ is independent of the MESO. The design of the feedback controller is entirely decoupled from the MESO. This characteristic is also preserved in the designed ADRC for current and position loops based on the MESO. This separation enables the independent adjustment of disturbance rejection performance via the MESO without impacting the setpoint tracking determined according to the feedback controller. In contrast, the traditional LESO does not possess this property, as the equivalent plant using the LESO is always coupled with the LESO.*

A fractional-order PD (FOPD) controller was designed as the feedback controller, which can be expressed as follows:

$$u_0 = k_p(r - \hat{x}_1) - k_d D^{\alpha-1}\hat{x}_2, \tag{32}$$

where $D^{\alpha-1}(\cdot)$ represents the fractional-order differential, and the order of the derivative is $\alpha - 1$. The Caputo definition of the fractional-order derivative was adopted in this paper. The nominal control system of the speed loop is shown in Figure 4. The parameters of FOPD were designed based on this nominal control system.

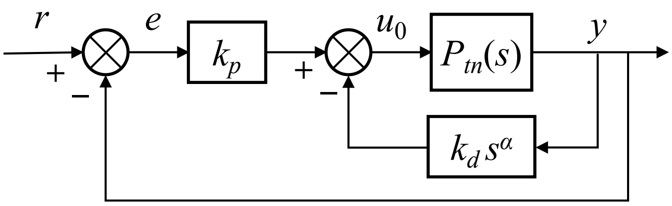

Figure 4. The nominal control system of the speed loop.

Per Figure 4, the open-loop transfer function is

$$G_{ol}(s) = \frac{k_p}{s^2 + k_d s^{\alpha}} = \frac{k_p}{s^{\alpha}(s^{2-\alpha} + k_d)}, \tag{33}$$

There is a fractional-order integrator in (33), and α should satisfy $\alpha \geq 1$ to ensure the steady-state error. Given the gain crossover frequency ω_{cn} and phase margin ϕ_m, the equations can be obtained as follows:

$$\begin{cases} |G_{on}(j\omega_{cn})| = \frac{k_p}{\sqrt{\omega_{cn}^4 + k_d^2\omega_{cn}^{2\alpha} - 2k_d\omega_{cn}^{2+\alpha}\cos(\alpha\pi/2)}} = 1 \\ \arg[G_{on}(j\omega_{cn})] = -\tan^{-1}\frac{\omega_{cn}^2\sin(\alpha\pi/2)}{k_d\omega_{cn}^{\alpha} - \omega_{cn}^2\cos(\alpha\pi/2)} - \frac{\alpha\pi}{2} = -\pi + \phi_m \end{cases}. \tag{34}$$

Given a specific α, the parameters of k_p and k_d for (32) can be obtained as follows:

$$\begin{cases} k_p = \frac{\omega_{cn}^2\sin(\alpha\pi/2)}{\sin(\phi_m + \alpha\pi/2)} \\ k_d = \frac{\omega_{cn}^{2-\alpha}\sin(\phi_m)}{\sin(\phi_m + \alpha\pi/2)} \end{cases}. \tag{35}$$

The choice of α is bounded as $\alpha \in [1,\ 2(\pi - \phi_m)/\pi)$ for a specific phase margin, ϕ_m. The choice of α is a trade-off between disturbance rejection and noise suppression.

The complementary sensitivity function of the nominal control system is

$$T_n(s) = \frac{G_{ol}(s)}{1 + G_{ol}(s)} = \frac{k_p}{s^2 + k_d s^{\alpha} + k_p}. \tag{36}$$

It is also the closed-loop transfer function of the nominal control system. The noise suppression specification defined by $T_n(s)$ determines the value of α, which is represented as

$$|T_n(j\omega_t)| \leq A_T \ \text{dB}, \tag{37}$$

where

$$|T_n(j\omega_t)| = \frac{k_p}{\sqrt{k_d^2\omega_t^{2\alpha} + (k_p - \omega_t^2)^2 + D_T}},$$

$$D_T = 2k_d\omega_t^{\alpha}(k_p - \omega_t^2)\cos(\alpha\pi/2).$$

Given the frequency ω_t, $|T_n(j\omega_t)|$ is calculated using (37) and (35) by sweeping α in $1 < \alpha < 2(\pi - \phi_m)/\pi$. Then, α is obtained from the curve of $|T_n(s)|$ with reference to α satisfying the gain limit of A_T dB. A flow chart of the design procedure for the speed loop is presented in Figure 5.

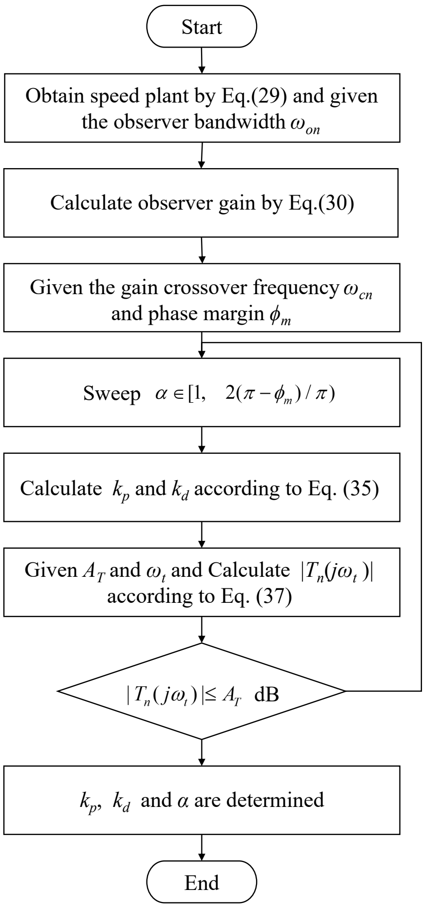

Figure 5. Flow chart of the design procedure for the speed loop.

The speed closed-loop transfer function can be obtained using (18) with $K_0 = [k_p \;\; k_d s^{1-\alpha} \;\; 1]$ as follows:

$$G_{cln}(s) = \frac{k_p}{s^2 + k_d s^\alpha + k_p}. \tag{38}$$

It is the same as the closed-loop transfer function of the nominal control system using (36).

3.4. Position Loop Design

Neglecting the fractional order, the designed speed closed-loop was approximated as an integer-order system. The difference in order was treated as part of the lumped disturbance. Therefore, according to (38) and (25), the controlled plant of the position loop can be represented as

$$P_p(s) = \frac{b}{s^3 + a_2 s^2 + a_1 s + a_0}, \tag{39}$$

where $b = k_p$, $a_2 = k_d$, $a_1 = k_p$, and $a_0 = 0$.

The MESO for the position loop can be designed based on (39), according to (5) and (6). Given the observer bandwidth ω_{op} , the observer gain can be obtained using (12) as follows:

$$\begin{cases} \beta_1 = & -a_2 + 4\omega_{op}, \\ \beta_2 = & -a_1 + a_2^2 - 4a_2\omega_{op} + 6\omega_{op}^2, \\ \beta_3 = & -a_0 + 2a_1a_2 - a_2^3 - 4a_1\omega_{op} + 4a_2^2\omega_{op} - 6a_2\omega_{op}^2 + 4\omega_{op}^3, \\ \beta_4 = & a_1^2 + 2a_0a_2 - 3a_1a_2^2 + a_2^4 - 4a_0\omega_{op} + 8a_1a_2\omega_{op} - 4a_2^3\omega_{op} \\ & -6a_1\omega_{op}^2 + 6a_2^2\omega_{op}^2 - 4a2\omega_{op}^3 + \omega_{op}^4. \end{cases} \tag{40}$$

The bandwidth parameterization method was used to tune the feedback controller for the position loop. Placing all the poles of the closed loop at $-\omega_{cp}$ allowed the parameter's value to be solved from (14) as follows:

$$k_1 = \omega_{cp}^3, k_2 = 3\omega_{cp}^2, k_3 = 3\omega_{cp}. \tag{41}$$

4. Simulation and Discussion

The mathematical models of the experimental PMSM were identified as

$$G_i(s) = \frac{403.48}{s + 153.57}, \tag{42}$$

$$G_n(s) = \frac{333.85}{s + 0.4889}. \tag{43}$$

Such a PMSM device was used for the subsequent simulation and analysis.

Three control strategies are presented for comparison: the traditional LESO-based ADRC [6], the proposed MESO-based ADRC with a PD feedback controller, and the proposed MESO-based ADRC with an FOPD feedback controller. The control strategies designed for comparison are listed in Table 2.

Table 2. Control strategies designed for comparison.

	Current Loop	Speed Loop	Position Loop
LESO-based	P-LESO	PD-LESO	PD-LESO
MESO-based	P-MESO	PD-MESO	PD-MESO
FOC- and MESO-based	P-MESO	FOPD-MESO	PD-MESO

4.1. Current Loop

The plant parameters can be determined as $a_0 = 153.57$ and $b = 403.48$ via (42). Given $\omega_{ci} = 1000$ rad/s and $\omega_{oi} = 5000$ rad/s, the parameters of the MESO-based ADRC for the current loop can be designed as $\beta_1 = 9846.43$, $\beta_2 = 2.3488 \times 10^7$, and $k_1 = 1000$. The parameters designed for the LESO-based ADRC are $\beta_1 = 10{,}000$, $\beta_2 = 2.5 \times 10^7$, and $k_1 = 1000$.

4.2. Speed Loop

The controlled plant of the speed loop is represented by (29), with $a_0 = 488.9$, $a_1 = 1000.49$, and $b = 3.34 \times 10^5$. The design specifications for the speed loop included $\omega_{cn} = 100$ rad/s, $\omega_{on} = 500$ rad/s, $\phi_m = 70^\circ$, $\omega_t = 1000$ rad/s, and $A_T = -24.8$ dB. Subsequently, the MESO for the speed loop could be designed.

Considering $\phi_m = 70^\circ$, the fractional order bound for FOPD can be calculated as $\alpha \in [1, 1.22)$. By sweeping α within this range, the parameters k_p and k_d can be determined using (35). The parameter curve for FOPD is illustrated in Figure 6a. As α approaches its upper bound, k_p increases rapidly. The gain of $T_n(s)$ at ω_t can be calculated using (37). The curve of $|T_n(j\omega_t)|$ with respect to α is depicted in Figure 6b. It indicates that the gain in $T_n(s)$ increases with a rising α, leading to a gradual decrease in the noise suppression ability. For $\alpha \in (1,\ 1.18]$, the constraint in (37) is satisfied. Hence, $\alpha = 1.18$ was selected to achieve better disturbance rejection performance.

The PD-LESO and PD-MESO controllers were also designed for comparison using the same design specifications. The parameters of the design controllers for the speed loop are shown in Table 3.

(1) Disturbance rejection and noise suppression for the ESO: When the estimation error is defined as $e_x = x - \hat{x}$, the dynamics of the estimation error can be obtained using (5) and (6) as follows:

$$\dot{e}_x = (A - LC)e_x + E\dot{d} - Ln. \tag{44}$$

where n is the sensor noise. By applying the Laplace transform to (44), the transfer function from d to e_{x3} ($e_{x3} = f - \hat{f}$) can be obtained as follows:

$$G_{ed}(s) = C_f[sI - (A - LC)]^{-1}Es, \tag{45}$$

The transfer function from n to e_{x3} can be derived as follows:

$$G_{en}(s) = C_f[sI - (A - LC)]^{-1}L, \tag{46}$$

where $C_f = [0\ 0\ \ \ldots\ \ 0\ 1]_{n+1}$. G_{ed} and G_{en} are used to evaluate the MESO's disturbance rejection and noise sensitivity, respectively. Therefore, $G_{ed}(s)$ and $G_{en}(s)$ for the speed loop can be obtained as follows:

$$G_{ed} = \frac{s^2 + \beta_1 s + \beta_2}{(s + \omega_{on})^3}, \tag{47}$$

$$G_{en} = \frac{\beta_3 s^2 - a_0\beta_2 s}{(s + \omega_{on})^3}. \tag{48}$$

The Bode plots of $G_{ed}(s)$ and $G_{en}(s)$ are depicted in Figure 7a,b. With the same observer bandwidth ω_{on}, Figure 7 illustrates that the MESO exhibits superior disturbance estimation performance compared to the LESO, while both maintain the same noise suppression performance. The disturbance estimation performance of the LESO improves as ω_{on} increases, but the noise suppression performance decreases simultaneously.

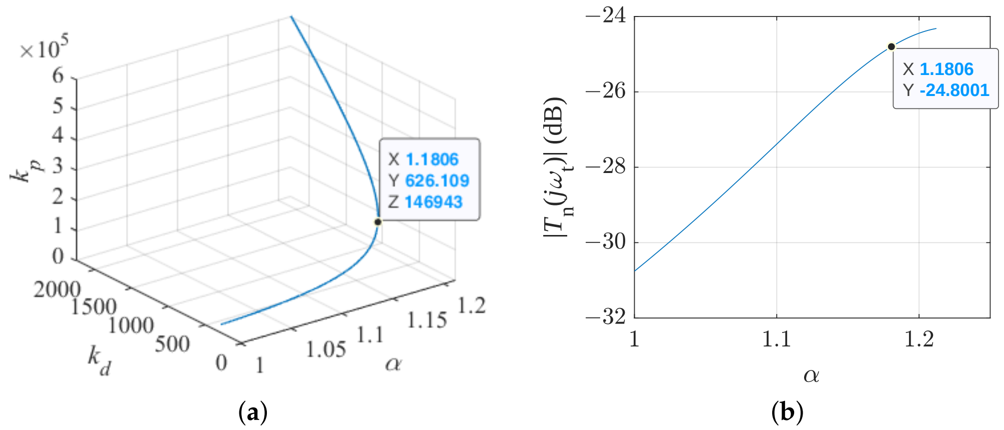

Figure 6. Curves for FOPD design: (**a**) parameters curve; (**b**) $|T_n(j\omega_t)|$ w.r.t. α.

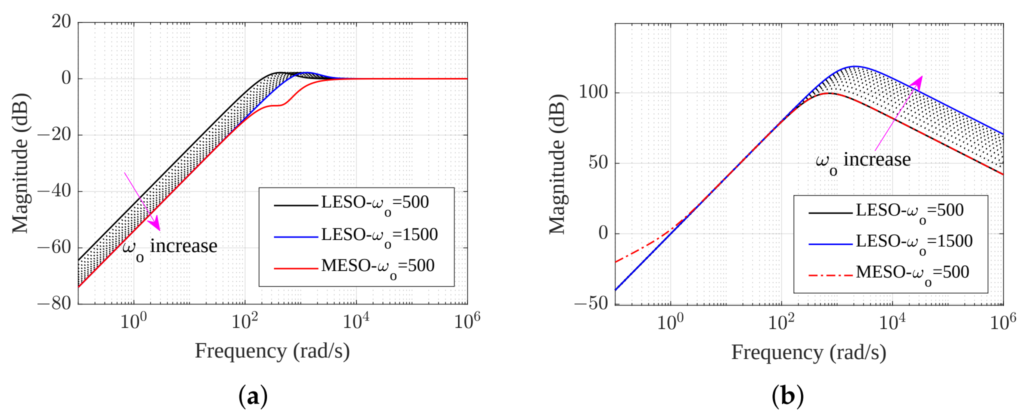

Figure 7. Frequency responses comparison of a different ESO for the speed loop: (**a**) disturbance estimation ; (**b**) noise suppression.

Table 3. Parameters of the designed controllers for the speed loop.

	k_1	k_2	α	β_1	β_2	$\beta_3(\times 10^8)$
PD-LESO	29,238.0	274.75	1	1500	750,000	1.25
PD-MESO	29,238.0	274.75	1	499.51	249,755	−1.2512
FOPD-MESO	144,897	618.93	1.18	499.51	249,755	−1.2512

Remark 4. *Since the MESO incorporates the plant information as the known part of the total disturbance, the burden of MESO tracking f is lower compared to the traditional LESO. It is well known that the selection of observer bandwidth involves a trade-off between disturbance estimation and noise sensitivity. Therefore, the MESO alleviates this conflict and achieves better disturbance estimation and noise suppression performance simultaneously compared to the LESO under a limited observer bandwidth.*

(2) The equivalent plant: The Bode plots of the equivalent plant are presented in Figure 8. It shows that the MESO-based equivalent plant is identical to the nominal plant, represented as $1/s^2$. However, the LESO-based equivalent plant differs significantly from the nominal plant. Although the differences between the equivalent plant and the nominal plant decrease as ω_{on} increases, the LESO becomes more sensitive to noise at a high ω_{on}.

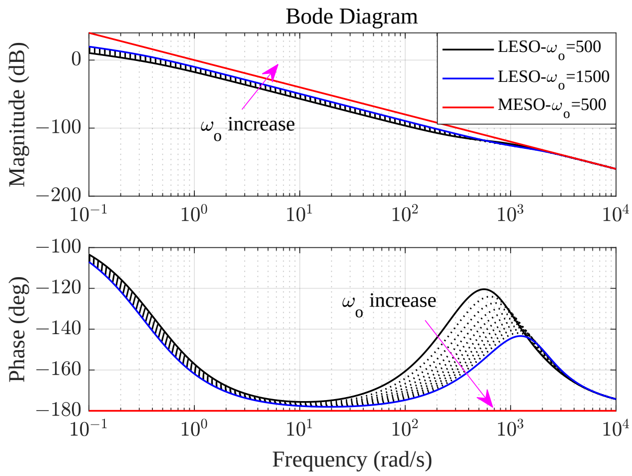

Figure 8. Bode plots of the equivalent plant for the speed loop.

(3) Open-loop Bode plots: Open-loop Bode plots are illustrated in Figure 9a. It is evident from the plots that the designed PD-MESO and FOPD-MESO met the design specifications, whereas the PD-LESO did not. Due to the significant difference between the LESO-based equivalent plant and the nominal plant, the designed PD feedback controller based on the nominal plant could not meet the design specifications in the real system. In the case of the FOPD-MESO, the gain at the low-frequency range increased with a rising α, leading to an improvement in the steady-state error. However, simultaneously, the gain in the high-frequency range also increased with a rising α, indicating a decrease in noise suppression performance.

(4) Closed-loop Bode plots: The closed-loop transfer function is identical to the complementary sensitivity function, as per (38) and (36). The Bode plots are depicted in Figure 9b. It is observed that the PD-MESO exhibited the lowest resonance peak. The resonance peak of the PD-LESO was notably higher than that of the other controllers. The resonance peak of the FOPD-MESO increased with a rising α, accompanied by an increase in the gain in the high-frequency range. The relative stability and noise suppression of the FOPD-MESO decreased as α increased.

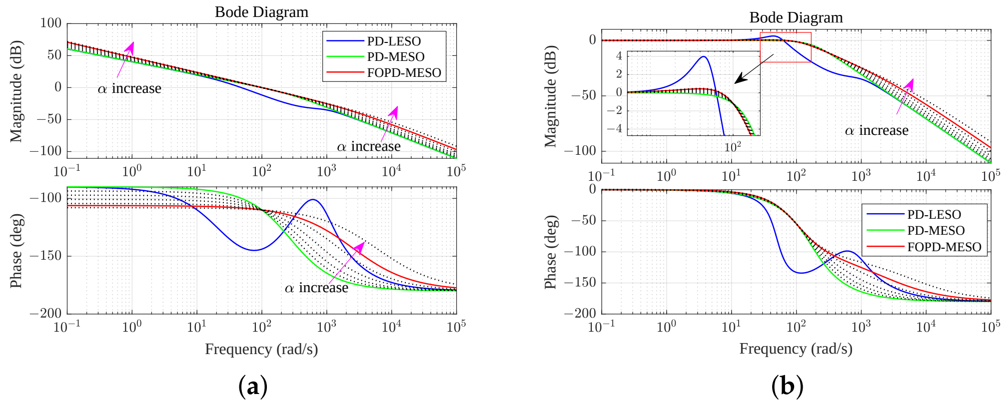

Figure 9. Bode plots of the transfer functions for the speed loop: (**a**) the open loop; (**b**) the closed loop.

(5) The disturbance rejection of the closed loop: According to (19), the disturbance transfer function of the speed loop is

$$G_{dn}(s) = \frac{b(\beta_2 + k_p)s + b(\beta_1 + s)(s^2 + k_d s^\alpha)}{(s^2 + k_d s^\alpha + k_p)(s + \omega_o)^3}. \tag{49}$$

Bode plots of the disturbance transfer function $G_{dn}(s)$ are presented in Figure 10. It is evident that the MESO-based ADRC exhibited superior disturbance rejection performance compared to the other controllers. Moreover, the disturbance rejection performance of the FOPD-MESO improved with an increasing α. Therefore, in addition to the MESO, the FOPD-MESO can enhance the disturbance rejection performance by adjusting α. The choice of α involves a trade-off between disturbance rejection and noise suppression.

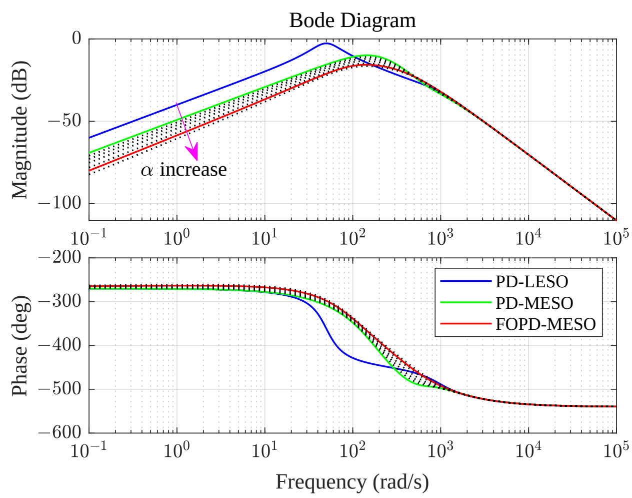

Figure 10. Bode plots of the disturbance transfer function for the speed loop.

(6) The disturbance rejection tuning with ω_{on} and α: Based on the analysis above, it can be concluded that the disturbance rejection performance of the FOPD-MESO can be simultaneously tuned by adjusting ω_{on} and α. To explore this property, the step responses with disturbance for various ω_{on} and α values are depicted in Figure 11a,b. Figure 11a demonstrates that the disturbance rejection performance improved as the value of ω_{on} increased, while the tracking performance remained unchanged. This verifies that the MESO-based ADRC satisfied the separation principle. The tracking performance was independent of the observer gain. Figure 11b illustrates that the disturbance rejection performance improved as α increased. However, the overshoot of the setpoint tracking also increased simultaneously. Therefore, the FOPD provides another tunable parameter α to enhance the disturbance rejection performance based on the MESO.

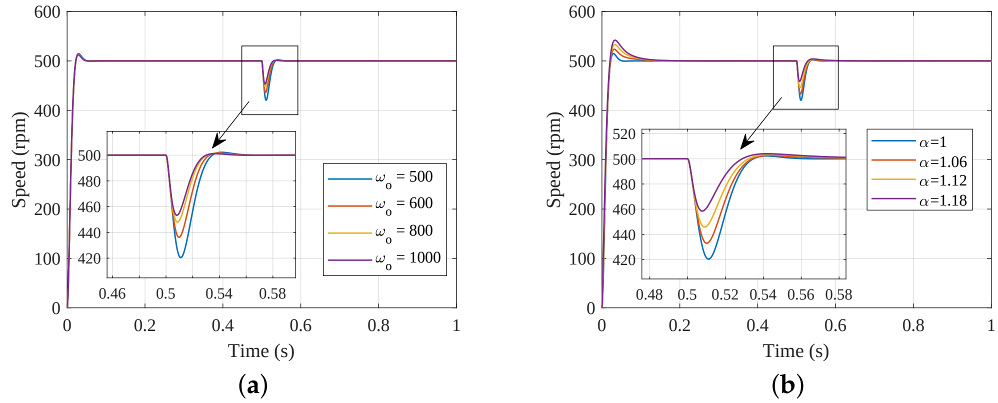

Figure 11. The step response of the MESO-based ADRC for the speed loop (simulation): (**a**) different ω_{on} values ($\alpha = 1$); (**b**) different α values ($\omega_o = 500$ rad/s).

(7) Step response comparison for different control strategies: The step response of the speed loop is depicted in Figure 12. It is evident that the MESO-based ADRC exhibited superior tracking and disturbance rejection. The PD-LESO exhibited a worse transient response compared to the other controllers. When a disturbance was applied, the speed drop of the FOPD-MESO was 8.3%, significantly less than the PD-MESO's 15.9%. Compared to the PD-MESO, the overshoot of the FOPD-MESO increased slightly from 3.0% to 8.4%. Therefore, the fractional order α can be adjusted to balance tracking and disturbance rejection performance.

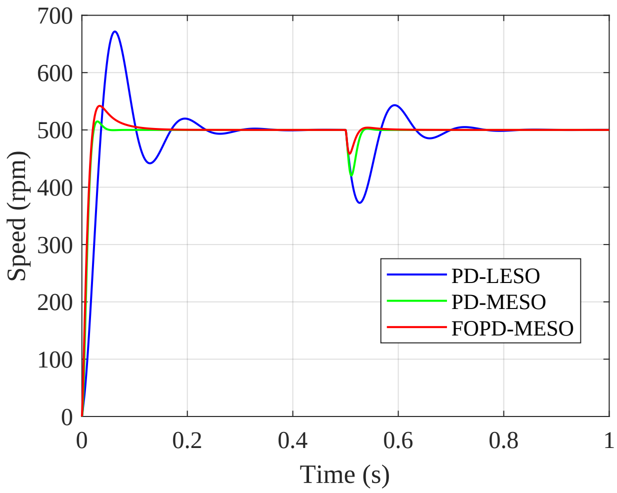

Figure 12. The step response comparison for the speed loop (simulation).

4.3. Position Loop

The approximate plant of the position loop can be determined using (39), with $b = 29{,}238.0$, $a_0 = 0$, $a_1 = 29{,}238.0$, and $a_2 = 274.747$. When the design specifications of the position loop are set as $\omega_{cp} = 50$ rad/s and $\omega_{op} = 250$ rad/s, PD-MESO and PD-LESO can be designed based on this plant. The parameters of the design controllers for the position loop are presented in Table 4.

Table 4. Parameters of the designed controllers for the position loop.

	k_1	k_2	k_2	β_1	β_2	$\beta_3(\times 10^6)$	$\beta_4(\times 10^8)$
PD-LESO	125,000	7500	150	1000	375,000	62.5	39.0625
PD-MESO	125,000	7500	150	725.252	146,500	1.04435	−6.64074

Figure 13 presents the step response of the position loop. It is evident that the LESO-based ADRC strategy exhibited a greater overshoot and position error when the disturbance was applied. This did not meet the design expectations, as the equivalent plant based on the LESO was significantly different from the nominal plant. However, the step response of the proposed MESO-based ADRC and FOC- and MESO-based ADRC could closely match the step response of the nominal system when using the same observer bandwidth. Additionally, the FOC- and MESO-based ADRC exhibited the smallest position error after disturbance input at 2.0%, compared to the MESO-based ADRC's 4.5%. Therefore, the simulation indicated the best disturbance rejection performance of the FOC- and MESO-based ADRC compared with the other controllers.

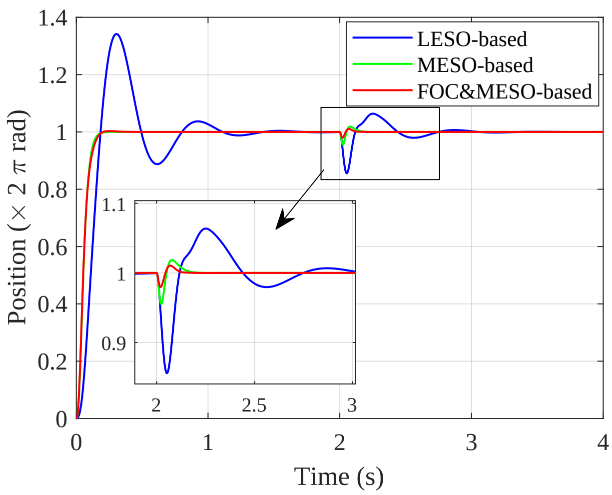

Figure 13. The step response comparison for the position loop (simulation).

5. Experimental Verification

5.1. Experimental Setup

Experimental validation was performed on a PMSM servo system, illustrated in Figure 14. The experimental setup consisted of essential components, including a PMSM, a servo drive, a DC generator, and a PC. The servo driver was powered via DSP-TMS320F28335. The structure of the PMSM position servo system based on field-oriented control is depicted in Figure 15. The control sampling frequencies for the current, speed, and position loops were 10 kHz, 5 kHz, and 2 kHz, respectively. The specifications of the PMSM are provided in detail in Table 5.

Figure 14. The experimental PMSM position servo system.

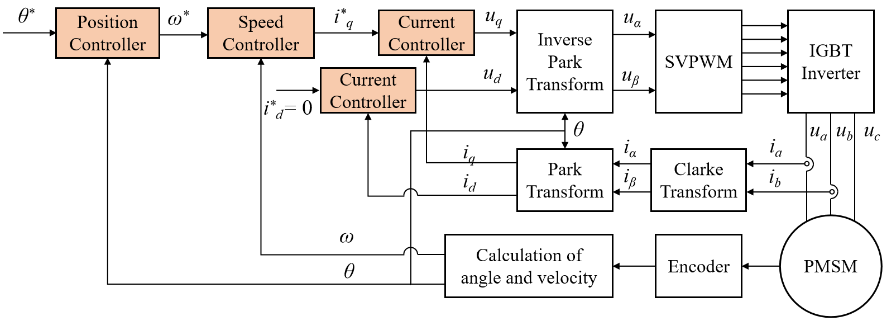

Figure 15. The structure of the PMSM position servo system based on field-oriented control.

Table 5. Specifications of the PMSM.

Parameters	Unit	Value
Rated power	kW	2.0
Rated speed	rpm	2000
Rated current	A	9.4
Line resistance	Ω	0.38
Line inductance	mH	2.48
Induced voltage coefficient	V/krpm	67.4
Moment of inertia	$\text{kg} \cdot \text{m}^2$	24.3×10^{-4}

5.2. Experimental Tests for the Speed Loop

The fractional-order differential $s^{0.18}$ was approximated using a five-order discrete transfer function obtained through the impulse response invariant discretization method of [16]:

$$s^{0.18} \approx \frac{N}{D}, \tag{50}$$

where

$$\begin{aligned} N &= z^5 - 3.05222z^4 + 3.43539z^3 - 1.71645z^2 + 0.352724z - 0.0193436, \\ D &= 0.248528z^5 - 0.708956z^4 + 0.730482z^3 - 0.321782z^2 + 0.0534573z - 0.00163956. \end{aligned} \tag{51}$$

The Bode plot of the approximated $s^{0.18}$ is shown in Figure 16. It can be seen that the approximated fractional-order operator matched the true Bode plot of $s^{0.18}$ around $\omega = 100$ rad/s, the gain crossover frequency of the speed loop, which means the approximated fractional-order ADRC could perform as the real fractional-order ADRC approximately.

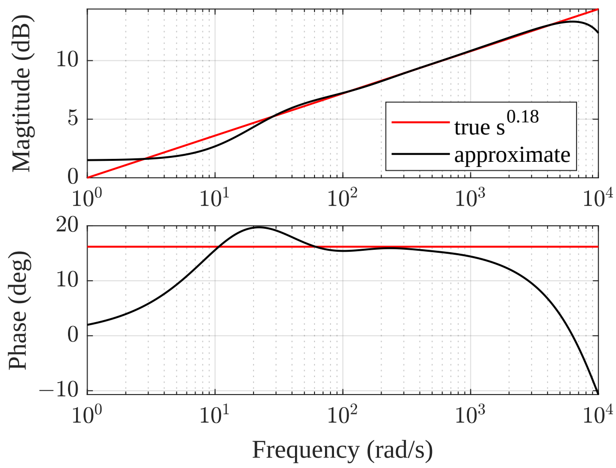

Figure 16. The Bode plot comparison of approximated and true $s^{0.18}$.

Figure 17a,b illustrates the step response of the PMSM's speed loop with varying values of ω_{on} and α. The experimental results validated the effectiveness of tuning disturbance rejection performance using ω_{on} and α, as observed in the simulation. It was observed that the tracking performance remained unaffected by the MESO bandwidth, while the disturbance rejection performance improved with an increasing ω_{on}. Furthermore, the disturbance performance improved with an increasing α, but it accompanied an increase in the overshoot.

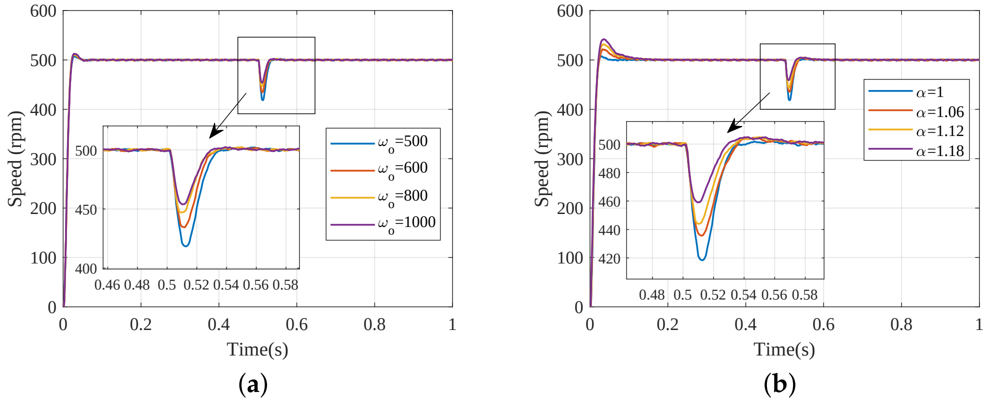

Figure 17. The step response of the MESO-based ADRC for the speed loop (experiment): (**a**) different ω_{on} values ($\alpha = 1$); (**b**) different α values ($\omega_{on} = 500$ rad/s).

Figure 18 presents the step response of the PMSM's speed loop employing different control methods. The performance indices are listed in Table 6. Consistent with the simulation results, the experimental results validated the findings. In comparison to the PD-LESO, the PD-MESO exhibited a significant improvement in both tracking and disturbance rejection performance using the same observer bandwidth. Additionally, the FOPD-MESO can enhance disturbance rejection performance by tuning the order of the feedback controller based on the MESO. The speed drop of the FOPD-MESO was 8.19%, versus the PD-MESO's 16.29%.

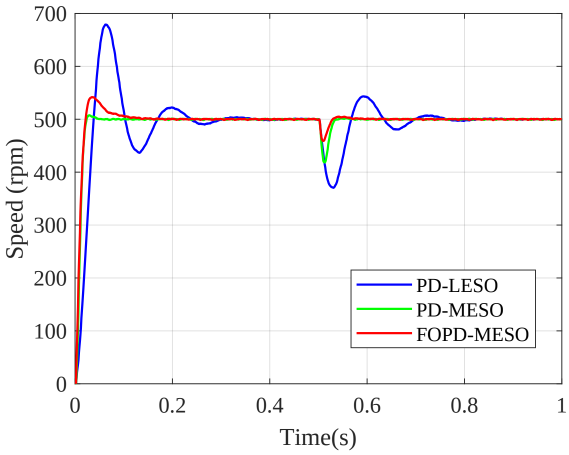

Figure 18. Step response comparison for the speed loop (experiment).

Table 6. Indices of the step responses for the speed loop.

	Overshoot	Settling Time	Speed Drop	Recovery Time
PD-LESO	35.75%	0.225 s	25.92%	0.181 s
PD-MESO	1.51%	0.0205 s	16.29%	0.029 s
FOPD-MESO	8.36%	0.085 s	8.19%	0.0238 s

5.3. Experimental Tests for the Position Loop

Figure 19 illustrates the step response of the PMSM's position loop. The legend names represent the different control strategies for comparison, which can be found in Table 2. Consistent with the simulation, the experimental results aligned with the expected outcomes. The setpoint tracking of the LESO-based ADRC exhibited a large overshoot, deviating significantly from the behavior of the nominal control system. In contrast, the setpoint tracking of the MESO-based and the FOC- and MESO-based ADRC aligned with the nominal control system. The disturbance rejection performance of the MESO-based ADRC was significantly improved compared to the LESO-based ADRC. Moreover, the FOC- and MESO-based ADRC further enhanced the disturbance rejection performance based on the MESO-based ADRC, When the disturbance was applied, the position error of the FOC- and MESO-based ADRC improved to 2.2 % from the MESO-based ADRC's 4.3%.

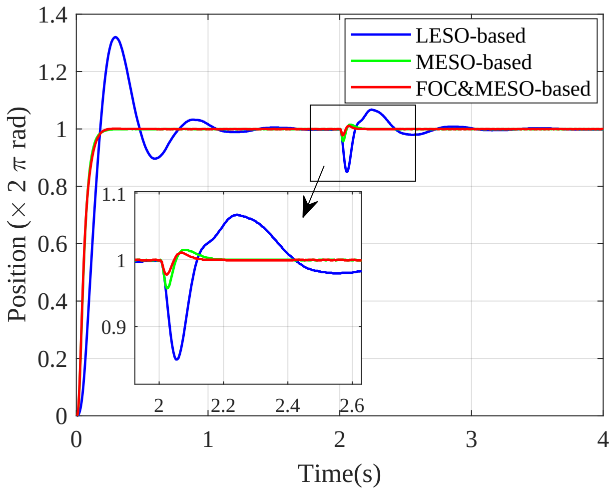

Figure 19. The step response comparison for the position loop (experiment).

6. Conclusions

This paper has proposed a cascade FOADRC architecture with an MESO for a PMSM position servo system. The MESO-based ADRC was designed for the current, speed, and position loops of the PMSM position servo system. Moreover, a fractional-order PD feedback controller was designed for the speed loop to further improve disturbance rejection performance on the basis of the MESO. The simulation and experimental verification were conducted on a PMSM servo platform. The results demonstrate that the proposed method achieved the desired tracking performance. Additionally, using the same observer bandwidth, the position error of the proposed strategy decreased to 2.25% when the disturbance was input, in contrast to the traditional LADRC's 14.9% and the MESO-based integer-order ADRC's 4.3%. The proposed method achieved superior tracking and disturbance rejection performance with a limited observer bandwidth.

Author Contributions: Conceptualization, Y.L., X.L. and Y.C.; methodology, S.W.; software, S.W. and H.G.; validation, S.W. and H.G.; formal analysis, S.W.; investigation, S.W.; writing—original draft preparation, S.W.; writing—review and editing, Y.L., X.L. and Y.C.; visualization, S.W.; supervision, Y.C.; project administration, Y.L. and X.L.; funding acquisition, Y.L. All authors have read and agreed to the published version of the manuscript.

Funding: This research was funded by the National Natural Science Foundation of China (grant number: 51975234).

Data Availability Statement: No new data were created or analyzed in this study.

Conflicts of Interest: The authors declare no conflicts of interest.

Abbreviations

PMSM	Permanent magnet synchronous motor
ADRC	Active disturbance rejection control
LADRC	Linear ADRC
PID	Proportional-integral-derivative
FOC	Fractional-order control
FOPD	Fractional-order proportional-derivative
FOADRC	Fractional-order ADRC
ESO	Extended state observer
GESO	Generalized ESO
MESO	Model-aided ESO

References

1. Wang, G.; Liu, R.; Zhao, N.; Ding, D.; Xu, D. Enhanced linear ADRC strategy for HF pulse voltage signal injection-based sensorless IPMSM drives. *IEEE Trans. Power Electron.* **2019**, *34*, 514–525. [CrossRef]
2. Chen, W.; Yang, J.; Guo, L.; Li, S. Disturbance-observer-based control and related methods —An overview. *IEEE Trans. Ind. Electron.* **2016**, *63*, 1083–1095. [CrossRef]
3. Liu, H.; Li, S. Speed control for PMSM servo system using predictive functional control and extended state observer. *IEEE Trans. Ind. Electron.* **2011**, *59*, 1171–1183. [CrossRef]
4. Alcántara, S.; Vilanova, R.; Pedret, C. PID control in terms of robustness/performance and servo/regulator trade-offs: A unifying approach to balanced autotuning. *J. Process. Control* **2013**, *23*, 527–542. [CrossRef]
5. Han, J. From PID to Active Disturbance Rejection Control. *IEEE Trans. Ind. Electron.* **2009**, *56*, 900–906. [CrossRef]
6. Gao, Z. Scaling and Bandwidth-Parameterization Based Controller Tuning. In Proceedings of the The 2003 American Control Conference, Denver, CO, USA, 4–6 June 2003; Volume 6, pp. 4989–4996.
7. Ren, L.; Mao, C.; Song, Z.; Liu, F. Study on Active Disturbance Rejection Control with Actuator Saturation to Reduce the Load of a Driving Chain in Wind Turbines. *Renew. Energy* **2019**, *133*, 268–274. [CrossRef]
8. Fareh, R.; Khadraoui, S.; Abdallah, M.Y.; Baziyad, M.; Bettayeb, M. Active Disturbance Rejection Control for Robotic Systems: A Review. *Mechatronics* **2021**, *80*, 102671. [CrossRef]
9. Sun, H.; Sun, Q.; Wu, W.; Chen, Z.; Tao, J. Altitude Control for Flexible Wing Unmanned Aerial Vehicle Based on Active Disturbance Rejection Control and Feedforward Compensation. *Int. J. Robust Nonlinear Control* **2020**, *30*, 222–245. [CrossRef]
10. Liu, J.; Sun, M.; Chen, Z.; Sun, Q. Output Feedback Control for Aircraft at High Angle of Attack Based upon Fixed-Time Extended State Observer. *Aerosp. Sci. Technol.* **2019**, *95*, 105468. [CrossRef]
11. Meng, Y.; Liu, B.; Wang, L. Speed Control of PMSM Based on an Optimized ADRC Controller. *Math. Probl. Eng.* **2019**, *2019*, 1074702. [CrossRef]
12. Wu, Z.; Zhou, H.; Guo, B.; Deng, F. Review and New Theoretical Perspectives on Active Disturbance Rejection Control for Uncertain Finite-Dimensional and Infinite-Dimensional Systems. *Nonlinear Dyn.* **2020**, *101*, 935–959. [CrossRef]
13. Li, D.; Ding, P.; Gao, Z. Fractional Active Disturbance Rejection Control. *ISA Trans.* **2016**, *62*, 109–119. [CrossRef] [PubMed]
14. Du, Y.; Cao, W.; She, J. Analysis and Design of Active Disturbance Rejection Control With an Improved Extended State Observer for Systems With Measurement Noise. *IEEE Trans. Ind. Electron.* **2023**, *70*, 855–865. [CrossRef]
15. Guo, B.; Bacha, S.; Alamir, M.; Hably, A.; Boudinet, C. Generalized integrator-extended state observer with applications to grid-connected converters in the presence of disturbances. *IEEE Trans. Control Syst. Technol.* **2020**, *29*, 744–755. [CrossRef]
16. Chen, P.; Luo, Y. A two-degree-of-freedom controller design satisfying separation principle with fractional-order PD and generalized ESO. *IEEE/ASME Trans. Mechatron.* **2021**, *27*, 137–148. [CrossRef]
17. Fu, C.; Tan, W. Tuning of linear ADRC with known plant information. *ISA Trans.* **2016**, *65*, 384–393. [CrossRef] [PubMed]
18. Fu, C.; Tan, W. Control of Unstable Processes with Time Delays via ADRC. *ISA Trans.* **2017**, *71*, 530–541. [CrossRef]
19. Zhou, R.; Tan, W. Analysis and Tuning of General Linear Active Disturbance Rejection Controllers. *IEEE Trans. Ind. Electron.* **2019**, *66*, 5497–5507. [CrossRef]
20. Liu, H.; Lin, W.; Liu, Z.; Buccella, C.; Cecati, C. Model Predictive Current Control With Model-Aid Extended State Observer Compensation for PMSM Drive. *IEEE Trans. Power Electron.* **2023**, *38*, 3152–3162. [CrossRef]
21. Cui, S.; Zhu, G.; Zhao, T. Linear Active Disturbance Rejection Control-Based Diagonal Recurrent Neural Network for Radar Position Servo Systems with Dead Zone and Friction. *Appl. Sci.* **2022**, *12*, 12839. [CrossRef]
22. Wang, Y.; Fang, S.; Hu, J. Active Disturbance Rejection Control Based on Deep Reinforcement Learning of PMSM for More Electric Aircraft. *IEEE Trans. Power Electron.* **2023**, *38*, 406–416. [CrossRef]
23. Zhang, Z.; Cheng, J.; Guo, Y. PD-Based Optimal ADRC with Improved Linear Extended State Observer. *Entropy* **2021**, *23*, 888. [CrossRef] [PubMed]
24. Dastjerdi, A.A.; Vinagre, B.M.; Chen, Y.; HosseinNia, S.H. Linear fractional order controllers; A survey in the frequency domain. *Annu. Rev. Control* **2019**, *47*, 51–70. [CrossRef]
25. Shi, X.; Chen, Y.; Huang, J. Application of Fractional-Order Active Disturbance Rejection Controller on Linear Motion System. *Control Eng. Pract.* **2018**, *81*, 207–214. [CrossRef]

26. Wang, S.; Gan, H.; Luo, Y.; Wang, X.; Gao, Z. Active Disturbance Rejection Control with Fractional-Order Model-Aided Extended State Observer. *ISA Trans.* **2023**, *142*, 527–537. [CrossRef]
27. Zhao, M.; Hu, Y.; Song, J. Improved Fractional-Order Extended State Observer-Based Hypersonic Vehicle Active Disturbance Rejection Control. *Mathematics* **2022**, *10*, 4414. [CrossRef]
28. Zhao, J.; Zhao, T.; Liu, N. Fractional-Order Active Disturbance Rejection Control with Fuzzy Self-Tuning for Precision Stabilized Platform. *Entropy* **2022**, *24*, 1681. [CrossRef]
29. Chen, P.; Luo, Y.; Peng, Y.; Chen, Y. Optimal Fractional-Order Active Disturbance Rejection Controller Design for PMSM Speed Servo System. *Entropy* **2021**, *23*, 262. [CrossRef]
30. Tian, G.; Gao, Z. Frequency Response Analysis of Active Disturbance Rejection Based Control System. In Proceedings of the 2007 IEEE International Conference on Control Applications, Singapore, 1–3 October 2007; pp. 1595–1599.